An Ordinary State-based Peridynamic Model for the Fracture of Zigzag Graphene Sheets

Xuefeng Liu [1], Xiaoqiao He [1,*], Jinbao Wang [2], Ligang Sun [3], Erkan Oterkus [4]

[1] Department of Architecture and Civil Engineering, City University of Hong Kong, Hong Kong

[2] School of Port and Transportation Engineering, Zhejiang Ocean University, Zhoushan, China

[3] Department of Mechanical and Biomedical Engineering, City University of Hong Kong, Hong Kong

[4] Department of Naval Architecture, Ocean and Marine Engineering, University of Strathclyde, Glasgow, UK

Abstract: This study develops an ordinary state-based peridynamic coarse-graining (OSPD-CG) model for the investigation of fracture in single layer graphene sheets (SLGS), in which the peridynamic (PD) parameters are derived through combining the PD model and molecular dynamics (MD) simulations from the fully atomistic system via energy conservation. The fracture failure of pre-cracked SLGS under uniaxial tension is studied using the proposed PD model. And the PD simulation results agree well with those from MD simulations, including the stress-strain relations, the crack propagation patterns and the average crack propagation velocities. The interaction effect between cracks located at the center and the edge on the crack propagation of the pre-cracked SLGS is discussed in detail. This work shows that the proposed PD model is much more efficient than the MD simulations and, thus, indicates that the PD-based method is applicable to study larger nanoscale systems.

* Corresponding author. E-mail: bcxqhe@cityu.edu.hk (Xiaoqiao He)

Keywords: Ordinary state-based Peridynamics; Coarse-graining; Molecular dynamics; Crack propagation; Graphene;

1. Introduction

Graphene sheets have gained increasing research interests for the reason that they are regarded as very promising materials in nanotechnology, electronics and other fields of material science and technology due to their unique and exceptional mechanical and electronic properties. For example, they can be used in display screens of mobile devices [1], to design ultra-capacitors with better performance than batteries [2] and for water desalination [3]. Especially in engineering, they are incorporated in composite materials as reinforcements [4, 5], which makes it of fundamental importance to understand its physical properties and behaviors beforehand because the mechanical performance of composites is affected significantly by the reinforcements. As a common phenomenon, failure may occur in the form of generation and growth of discontinuities such as cracks in such structures when they are under certain loading conditions. Therefore, it is of great significance to take this feature into consideration and understand the damage process or the way of crack growth sufficiently. Currently, numerical methods are the most favored ways for damage prediction due to their high efficiency and low cost.

Traditionally, two main types of approaches are employed to study the mechanical behavior of nanostructures such as graphene sheets and carbon nanotubes. The first one is based on the Classical Continuum Mechanics (CCM) theory which has been used in many studies to investigate the mechanical characters of graphene sheets [6-8].

Kitipornchai et al. [6] and He et al. [7] investigated the resonance phenomena of multi-layered graphene sheets. In their study, an explicit formula was derived to describe the van der waals (vdW) interaction between any two layers of graphene sheets. Based on the derived formula, a continuum-plate model was used for the study of the vibration of multi-layer graphene sheets. Reddy et al. [8] studied the elastic properties of finite sized graphene and found the elastic constants of the graphene sheet conform to orthotropic material behavior. In addition, Zou et al. [9] derived close-form expressions of the Young's moduli and the fracture stresses of graphene. Zhang et al. [10] proposed a continuum model based on the triangular lattice to accurately capture the stress and displacement fields of defects in single crystalline graphene and to design various 3D curved graphene structures. The second type of methods to analyze graphene is based on the atomistic simulation, such as the classical MD simulation with which the bond breaking can be presented. With this method, Zhao et al. [11] , Ansari et al. [12], Wang et al. [13] and Dewapriya et al. [14] studied the effects of temperature, strain-rate and defects on the fracture mechanisms of graphene sheets. Zhao et al. [11] showed that graphene can be a strong material even when subjected to variations in temperature, strain rate, and cracks and Dewapriya et al [14] found the central crack can be arrested by holes at certain positions in graphene. Zhang et al. [15] also reported that the fracture of nanocrystalline graphene is insensitive to the flaws. Detailed literature review about graphene can be found in the papers by Zhang et al. [16] and Rajasekaran et al. [17].

Although traditional CCM-based methods, such as finite element method (FEM) [18, 19], extended finite element method (XFEM) [20] and so on, are widely adopted,

they may fail to apply in discontinuous problems such as fracture failure due to the fact that the traditional approaches are based on the assumption of continuum media. The MD method can be used for the discretized atomic system. But compared with the traditional continuum-based method, this method is not practical for real-life structures due to its high computational cost for the simulation of large nano-scale systems. To save computational efforts in MD simulation, coarse-grained MD (CGMD) methods were proposed to study mechanical properties of graphene sheets [21-23]. However, they still work under MD framework and the computational efficient is limited. Thus, a new continuum-based theory, i.e. PD theory which was proposed by Silling [24], may be an alternative method for the discontinuous problems. It was originally known as "Bond-based PD (BPD) theory" and generalized as "State-based PD (SPD) theory" [25] afterwards.

To date, PD theory has been adopted successfully for damage prediction in various specific problems. Silling [26] simulated a Kalthoff-Winkler experiment in which a plate with two parallel notches was under impact load and successfully captured the angle of crack growth in the experiment. Ha and Bobaru [27] successfully captured the crack branching characteristics which agree well with experiments. Vazic et al. [28] investigated interactions between a macro-crack and many other micro-cracks and found combinations of micro-cracks can slow down the propagation of a macrocrack. Wang et al. [29] studied the crushing failure of ice under the action of a rigid cylinder and showed the crushing forces are on the same order as experimental data. Lai et al. [30] proposed a PD formulation for simulating geomaterial fragmentation under

impulsive loading. At micro-scale, Agwai et al. [31] applied PD theory to predict crack paths in multilayer thin film structures of electronic packages and showed that the results compare well with the experiments. Taylor et al. [32] simulated the formation of spontaneous ruptures in supported phospholipid double bilayer bio-membranes using PD modeling and concluded that pinning sites may indirectly determine the rupture morphology of membranes. Zhu et al. and De Meo et al. [33, 34] also modeled granular fracture in polycrystalline material with size of micrometer scale and successfully captured the trans- and inter-granular failure modes. Owing to the length-scale parameter, horizon, in PD theory, it is capable of capturing phenomena occurring at different length scales, including the nano-scale [35]. For example, Silling et al. [36] proposed 3D PD models for nanofiber networks and carbon nanotube reinforced composites in which vdW forces are included. The effect of vdW forces on the mechanical behavior, strength, and toughness properties of nanofiber networks under stretch deformation was also investigated by Bobaru et al. [37, 38], and they found fiber reorientation and accretion control the deformation of nanofiber networks. Celik et al. [39] studied the mechanical characterization of ultra-thin films under nano-indentation. Ebrahimi et al. [40] analyzed the nano-scale friction and wear behavior of amorphous carbon thin films, in which the obtained material properties are shown to be in good agreement with published experimental results. For more detailed introduction to PD theory and its applications the readers can be referred to Refs. [41-43].

Above works show that PD theory can be another efficient method compared with MD and CGMD to study the mechanical characteristics of larger nanoscale graphene.

Heretofore, some PD-based studies on graphene have been performed. Martowicz et al. [44] studied elastic wave propagation in graphene nanoribbons and discussed its capability of recovering the physical nature of the reactions at the atomic scale using dispersion characteristics. Oterkus et al. [35] investigated the fracture property in graphene sheets based on a linear elastic BPD model. However, the original PD theory is based on the CCM theory, which makes it unsuitable to study the mechanical characters of nanoscale materials. To overcome such limitation, an OSPD-CG model is developed in this work based on the fully atomistic system to study the mechanical characteristics of SLGS.

In this study, the continuum-based OSPD-CG model is introduced first by using a nonlinear material model. Then the approach to determine the PD parameters in the OSPD-CG model for the modeling of fracture in SLGS is presented. Next the OSPD-CG model is validated using the fully atomistic MD simulations. Finally, fracture behaviors and mechanisms in SLGS with different defects under uniaxial tensile loading are investigated and analyzed based on the OSPD-CG model.

2. OSPD-CG model of SLGS

In PD theory, it assumes that a continuum medium is composed of infinitesimally small material points and each material point interacts with other points inside its influence domain, *H*, called horizon with radius of δ (Figure 1). Each pair of material points interact through a PD bond and the interaction is defined by PD force density vectors in which all the constitutive information about the material is contained. Figure 1 shows the configurations before and after deformation, in which $\mathbf{x}_k$, $\mathbf{x}_j$ and $\mathbf{y}_k$, $\mathbf{y}_j$ stand for

the position vectors of material points k and j in the undeformed and deformed configurations, respectively. $\boldsymbol{t}_{kj}$ represents the PD force density vector on material point k from point j. Similarly, the PD force density vector applied on material point j by point k is $\boldsymbol{t}_{jk}$.

The PD equation of motion of a material point k at time t can be obtained by summing all PD forces acting on it and expressed as [43]

$$\rho_k \ddot{\mathbf{u}}_k = \sum_{j=1}^{N} \left(\mathbf{t}_{kj} - \mathbf{t}_{jk}\right) V_j + \mathbf{b}_k \tag{2.1}$$

in which $\mathbf{t}_{kj} - \mathbf{t}_{jk}$ can be seen as the net PD force density vector acting on material point k, ρ_k is the density, $\ddot{\mathbf{u}}_k$ is the acceleration, $\mathbf{b}_k$ is the body force density, N is the number of material points inside the horizon of the material point k and V_j represents the volume of material point j. The PD force density vectors can be expressed by the corresponding strain energy density function, W, as

$$\mathbf{t}_{kj} = \frac{1}{V_j} \frac{\partial W_k}{\partial(|\mathbf{y}_j - \mathbf{y}_k|)} \frac{\mathbf{y}_j - \mathbf{y}_k}{|\mathbf{y}_j - \mathbf{y}_k|} \tag{2.2}$$

$$\mathbf{t}_{jk} = -\frac{1}{V_k} \frac{\partial W_j}{\partial(|\mathbf{y}_j - \mathbf{y}_k|)} \frac{\mathbf{y}_j - \mathbf{y}_k}{|\mathbf{y}_j - \mathbf{y}_k|} \tag{2.3}$$

where V represents the volume of corresponding material point. $|\cdot|$ denotes the length of the corresponding vector. According to ref. [57], the nonlinear elastic strain energy density of can be expressed in term of the strain invariants as

$$\begin{aligned} U = {} & \frac{\nu E}{2(1-\nu^2)} \mathrm{Tr}(\boldsymbol{\epsilon})^2 + \frac{E}{2(1+\nu)} \mathrm{Tr}(\boldsymbol{\epsilon}^2) + \frac{1}{4}(C_{111} - C_{112}) \mathrm{Tr}(\boldsymbol{\epsilon}) \mathrm{Tr}(\boldsymbol{\epsilon}^2) \\ & + \frac{1}{4}\left(C_{112} - \frac{1}{3} C_{111}\right) \mathrm{Tr}(\boldsymbol{\epsilon})^3 \end{aligned} \tag{2.4}$$

where the Young's modulus E and the Poisson's ratio ν are two linear elastic constants and C_{111} and C_{112} are two nonlinear elastic constants. According to ref. [45],

the PD integral form of the strain invariants in equation (2.4) can be written as

$$\mathrm{Tr}(\boldsymbol{\epsilon}) = \theta \tag{2.5}$$

$$\mathrm{Tr}(\boldsymbol{\epsilon}^2) = \frac{1}{2}(4S - \theta^2) \tag{2.6}$$

Substituting equations (2.5) and (2.6) into equation (2.4), the PD strain energy density of material point *k* can be obtained as

$$\begin{aligned} W_k = &\left[\left(\frac{3}{8}C_{112} - \frac{5}{24}C_{111}\right)\theta_k + \frac{E(3\nu-1)}{4(1-\nu^2)}\right]{\theta_k}^2 \\ &+ \left[\frac{1}{2}(C_{111} - C_{112})\theta_k + \frac{E}{1+\nu}\right]S_k \end{aligned} \tag{2.7}$$

Wherein the dilatation term θ_k and the stretching term S_k are expressed as [45]

$$\theta_k = \frac{2}{m}\sum_{j=1}^{N} w_{kj}\left(|\mathbf{y}_j - \mathbf{y}_k|\Lambda_{kj} - |\mathbf{x}_j - \mathbf{x}_k|\right)|\mathbf{x}_j - \mathbf{x}_k|V_j \tag{2.8}$$

$$S_k = \frac{2}{m}\sum_{j=1}^{N} w_{kj}\left(|\mathbf{y}_j - \mathbf{y}_k|\Lambda_{kj} - |\mathbf{x}_j - \mathbf{x}_k|\right)^2 V_j \tag{2.9}$$

in which w_{kj} is an influence function to determine the influence of material points away from the current material point *k*. And according to ref. [43], it can be known

$$w_{kj} = \frac{\delta}{|\mathbf{x}_j - \mathbf{x}_k|} \tag{2.10}$$

$$\Lambda_{kj} = \frac{\mathbf{y}_j - \mathbf{y}_k}{|\mathbf{y}_j - \mathbf{y}_k|} \cdot \frac{\mathbf{x}_j - \mathbf{x}_k}{|\mathbf{x}_j - \mathbf{x}_k|} \tag{2.11}$$

Then the parameter m can be calculated as [45]

$$m = \frac{2}{3}\pi h \delta^4 \tag{2.12}$$

Finally, a general form of the strain energy density of material point *k* can be obtained as equation (2.13) which is consistent with the form in ref. [43].

$$W_k = (a_1\theta_k + a_0){\theta_k}^2 + (b_1\theta_k + b_0)\sum_{j=1}^{N} w_{kj}\left(|\mathbf{y}_j - \mathbf{y}_k|\Lambda_{kj} - |\mathbf{x}_j - \mathbf{x}_k|\right)^2 V_j \tag{2.13}$$

in which a_1, a_0, b_1 and b_0 are PD parameters. Comparing equations (2.13) and (2.7),

it can be known that the PD parameters are related with the elastic constants and evaluated as

$$a_1 = \frac{3}{8} C_{112} - \frac{5}{24} C_{111} \tag{2.14}$$

$$a_0 = \frac{E(3\nu - 1)}{4(1 - \nu^2)} \tag{2.15}$$

$$b_1 = \frac{3}{2\pi h \delta^4} (C_{111} - C_{112}) \tag{2.16}$$

$$b_0 = \frac{3E}{\pi h \delta^4 (1 + \nu)} \tag{2.17}$$

Analogously, the PD strain energy density for material point *j* can be derived as well.

According to the assumption in PD theory, the SLGS is composed of infinitesimally small material points and each material point consists of a cluster of atoms, for which the current model is called the OSPD-CG model. In an early study, Silling [46] proposed a linear BPD-CG method, which could accurately reproduce the effective elastic properties of a composite as well as the effect of a small defect in a homogeneous medium. Based on a linear material model, Oterkus et al. [35] simulated the fracture of SLGS using peridynamics and captured the crack branching behavior in SLGS, but the final fracture pattern was different from the fully atomistic MD simulation results due to the nonlinear material property of SLGS. Therefore, the nonlinear OSPD-CG model (Equation (2.13)) is established and it is more applicable to the physical nonlinear material, i.e. SLGS.

According to equations (2.2) and (2.3), PD force density expressions can also be written as

$$\mathbf{t}_{kj} = w_{kj}\left\{\bar{d}\Lambda_{kj}\left|\mathbf{x}_j - \mathbf{x}_k\right|\left[3a_1{\theta_k}^2 + 2a_0\theta_k + b_1\sum_{j=1}^{N} w_{kj}\left(\left|\mathbf{y}_j - \mathbf{y}_k\right|\Lambda_{kj} - \left|\mathbf{x}_j - \mathbf{x}_k\right|\right)^2 V_j\right] + 2(b_1\theta_k + b_0)\Lambda_{kj}\left(\left|\mathbf{y}_j - \mathbf{y}_k\right|\Lambda_{kj} - \left|\mathbf{x}_j - \mathbf{x}_k\right|\right)\right\}\frac{\mathbf{y}_j - \mathbf{y}_k}{\left|\mathbf{y}_j - \mathbf{y}_k\right|} \tag{2.18}$$

$$\mathbf{t}_{jk} = -w_{jk}\left\{\bar{d}\Lambda_{jk}\left|\mathbf{x}_k - \mathbf{x}_j\right|\left[3a_1{\theta_j}^2 + 2a_0\theta_j + b_1\sum_{j=1}^{N} w_{jk}\left(\left|\mathbf{y}_k - \mathbf{y}_j\right|\Lambda_{jk} - \left|\mathbf{x}_k - \mathbf{x}_j\right|\right)^2 V_k\right] + 2(b_1\theta_k + b_0)\Lambda_{jk}\left(\left|\mathbf{y}_k - \mathbf{y}_j\right|\Lambda_{jk} - \left|\mathbf{x}_k - \mathbf{x}_j\right|\right)\right\}\frac{\mathbf{y}_j - \mathbf{y}_k}{\left|\mathbf{y}_j - \mathbf{y}_k\right|} \tag{2.19}$$

where $\bar{d}$ is a PD parameter which is equal to

$$\bar{d} = \frac{3}{\pi h \delta^4} \tag{2.20}$$

(a) PD parameters in the OSPD-CG model

Equations (2.14~2.17) show that the PD parameters can be determined if the linear and nonlinear elastic moduli are known. The PD parameters in the general PD strain energy density expression also can be determined through calibration [43]. At present, two calibration ways are popular to determine the PD parameters. These are strain energy density-based [43] and stress-based [47] methods. The difference between these two methods is that the stress-based method is performed in the PD discretized model while the strain energy density-based one is more general. In this work, the strain energy density-based method is employed. However, different from the general approach, the PD parameters are derived by equating the PD strain energy density with the one obtained from the fully atomic scale system rather than the CCM counterpart.

(i) Strain energy density in the OSPD-CG model

Figure 2 shows the fully atomistic SLGS model, the corresponding OSPD-CG model and the states after deformation under different loading conditions.

Through MD simulations, it is found that the nonlinear material property of the fully atomistic SLGS can be well characterized by the strain energy density expressed with a third order function. Thus, the strain energy density W_k^{PD} of material point k in the PD model under biaxial expansion with strain of ε can be expressed as

$$\begin{aligned} W_k^{PD} &= (2a_1\varepsilon + a_0)(2\varepsilon)^2 + (2b_1\varepsilon + b_0)\int_0^{\delta}\int_0^{2\pi}\frac{\delta}{\xi}(\varepsilon\xi)^2 h\xi d\theta d\xi \\ &= 4\left(2a_1 + \frac{1}{3}b_1\pi h\delta^4\right)\varepsilon^3 + 2\left(2a_0 + \frac{1}{3}b_0\pi h\delta^4\right)\varepsilon^2 \end{aligned} \tag{2.21}$$

Under uniaxial extension with strain of ε, the strain energy density W_k^{PD} of material point k in the PD model is derived as

$$\begin{aligned} W_k^{PD} &= (a_1\varepsilon + a_0)\varepsilon^2 + (b_1\varepsilon + b_0)\int_0^{\delta}\int_0^{2\pi}\frac{\delta}{\xi}[\varepsilon\xi(\cos\theta)^2]^2 h\xi d\theta d\xi \\ &= \left(a_1 + \frac{1}{4}b_1 h\pi\delta^4\right)\varepsilon^3 + \left(a_0 + \frac{1}{4}b_0 h\pi\delta^4\right)\varepsilon^2 \end{aligned} \tag{2.22}$$

Under shear deformation with strain of γ, the strain energy density W_k^{PD} of material point k in the PD model is calculated as

$$W_k^{PD} = \int_0^{\delta}\int_0^{2\pi} b_0\frac{\delta}{\xi}(\sin\theta\cos\theta\,\gamma\xi)^2 h\xi d\theta d\xi = \frac{b_0}{12}\pi h\delta^4\gamma^2 \tag{2.23}$$

Note that $\xi = |\mathbf{x}_j - \mathbf{x}_k|$ in above equations and that a_0, a_1, b_0, and b_1 are PD parameters which need to be determined in the OSPD-CG model.

(ii) Strain energy density in the fully atomistic model

To obtain the PD parameters in the OSPD-CG model, a fully atomistic zigzag SLGS cell with size of approximately $15\text{nm} \times 15\text{nm}$ is considered to calculate the

corresponding strain energy densities by performing MD simulations under three loading conditions, biaxial expansion, uniaxial extension and simple shear. In this work the zigzag SLGS cell is chosen and in MD simulations, the SLGS cell is homogeneously deformed with a strain rate of 1×10^7/s according to the schematics of the three loading conditions shown in figure 3, respectively. Periodic boundary conditions are applied in x and y directions to avoid the free boundary effect and the temperature is 0K in the MD simulations. Besides, bond interactions between pairs of atoms and angle interactions between triplets of atoms in the MD simulations are computed based on morse bond potential and harmonic angle potential [48], respectively.

As the strain energy density of the SLGS cell may be different when the strain rate or the cell size changes, different strain rates (i.e. 1×10^6/s, 1×10^7/s, 1×10^8/s, and 1×10^9/s) and different cell sizes (i.e. 8nm×8nm, 15nm×15nm and 30nm×30nm) are considered in the MD simulations. And it shows that the strain rate and the cell size almost have no effect on the strain energy density. Based on MD simulations, the relationships between the strain energy density and strain of the fully atomistic SLGS cell under three loadings are obtained and fitted with linear least square method as presented in figure 4. In the figure, the strain energy density W_k^A in the fully atomistic model under biaxial expansion with strain of ε is obtained as

$$W_k^A = -2.219\times 10^{12}\varepsilon^3 + 1.131\times 10^{12}\varepsilon^2 \qquad (2.24)$$

Under uniaxial extension with strain of ε, the strain energy density W_k^A in the fully atomistic model is expressed as

$$W_k^A = -5.108 \times 10^{11}\varepsilon^3 + 4.478 \times 10^{11}\varepsilon^2 \quad (2.25)$$

Similarly, under shear loading with strain of γ, the strain energy density W_k^A in the fully atomistic model is

$$W_k^A = 1.606 \times 10^{11}\gamma^2 \quad (2.26)$$

(iii) Determination of PD parameters

The strain energy density in the OSPD-CG model under different loading conditions should be identical with that in the fully atomistic model. Thus, in the case of biaxial expansion, equating equations (2.21) and (2.24) yields

$$4a_0 + \frac{2}{3}\pi b_0 h\delta^4 = 1.131 \times 10^{12} \quad (2.27)$$

$$8a_1 + \frac{4}{3}\pi b_1 h\delta^4 = -2.219 \times 10^{12} \quad (2.28)$$

In the case of uniaxial extension, equating equations (2.22) and (2.25) results in

$$a_0 + \frac{1}{4}\pi b_0 h\delta^4 = 4.478 \times 10^{11} \quad (2.29)$$

$$a_1 + \frac{1}{4}\pi b_1 h\delta^4 = -5.108 \times 10^{11} \quad (2.30)$$

In the case of shear, equating equations (2.23) and (2.26), the following relationship can be obtained as

$$\frac{1}{12}\pi b_0 h\delta^4 = 1.606 \times 10^{11} \quad (2.31)$$

Finally, the PD parameters in the OSPD-CG model of SLGS can be derived from equations (2.20) and (2.27-2.31) and are summarized and listed in Table I.

(b) Damage criteria in the OSPD-CG model

Damage is introduced in PD equations of motion by eliminating the force density vectors between material points in an irreversible way. One general and simple damage criterion is the critical stretch-based one [49] which is based on the stretch of the PD

bond between material points *k* and *j*, i.e. s_{kj}. In addition, Foster et al. [50] proposed an energy-based damage criterion for a more complex PD model. In some cases, the critical stretch or critical energy may be difficult to determine theoretically. Then, combination of PD simulations and experiments may be required to obtain the critical values [43].

$$s_{kj} = \frac{|\mathbf{y}_j - \mathbf{y}_k| - |\mathbf{x}_j - \mathbf{x}_k|}{|\mathbf{x}_j - \mathbf{x}_k|} \tag{2.32}$$

In this study, the critical stretch-based damage criterion is adopted for simplicity, in which a history-dependent scalar value is introduced to determine the damage initiation [49] and written as

$$\mu_{kj} = \begin{cases} 1 & s_{kj} < s_c \\ 0 & s_{kj} \geq s_c \end{cases} \tag{2.33}$$

When the stretch s_{kj} exceeds the critical value s_c, the parameter μ_{kj} renders the corresponding force density vector to be zero, which means the PD bond breaks and damage occurs. The critical stretch of PD bonds s_c can be derived from the critical energy release rate G_c [49]. According to equation (2.1), the PD force density of one single PD bond *kj* can be expressed as $\mathbf{t}_{kj} - \mathbf{t}_{jk}$ which can be obtained from equations (2.18) and (2.19). Thus for one single PD bond *kj* with original length of ξ due to bond stretch of s_c, the induced bond energy can be approximately calculated as equation (2.34) by ignoring the dilatation terms.

$$E_{PD0} = \int_0^{s_c} 4w_{kj} b_0 \left(|\mathbf{y}_j - \mathbf{y}_k| - |\mathbf{x}_j - \mathbf{x}_k|\right) \xi ds_{kj} = 2b_0 \delta \xi {s_c}^2 \tag{2.34}$$

According to the method to determine the critical stretch in [49], all PD bonds crossing the crack surface in figure 5 should be broken due to the formation of the crack surface and the fracture energy per unit fracture area or the energy release rate in PD can be

obtained by integrating the energy of each bond which connects with material point k along the line with $0 \leq z \leq \delta$ and crosses the crack surface at the same time. Thus, the critical energy release rate in PD can be calculated as

$$E_{PDc} = 2\int_0^{\delta}\int_z^{\delta}\int_0^{\cos^{-1}(Z/\xi)} E_{PD0}\, h\xi d\phi\, d\xi\, dz = b_0 h\delta^5 {s_c}^2 \tag{2.35}$$

Besides, the critical energy release rate G_c in fully atomistic MD simulation can be obtained by equation (2.36).

$$G_c = \frac{W_t - W_{t+\Delta t}}{A} \tag{2.36}$$

in which $W_t - W_{t+\Delta t}$ is the energy difference before and after the formation of crack surface with area of A. The critical energy release rate in PD should be identical to that in fully atomic system, namely,

$$E_{PDc} = G_c \tag{2.37}$$

Solving the equations above, the value of the critical stretch can be expressed as

$$s_c = \sqrt{\frac{G_c}{b_0 h\delta^5}} \tag{2.38}$$

Additionally, in order to show damage formation inside a body (i.e. the dynamic in-plane fracture process in SLGS), a local damage index is introduced and defined as the ratio of the number of broken interactions to the total number of initial interactions of a material point with its neighbors inside its horizon (Equation (2.39)).

$$\varphi_k = 1 - \frac{\sum_{j=1}^{N} \mu_{kj} V_j}{\sum_{j=1}^{N} V_j} \tag{2.39}$$

3. Numerical simulation of fracture in SLGS

(a) Problem descriptions

Crack branching behaviors have been observed in graphene in the experiment [51] and

such phenomena were also found in zigzag SLGS in fully atomistic MD simulations in Ref. [52]. Therefore, in this work the newly developed OSPD-CG model is employed to study the fracture of the pre-cracked zigzag SLGS under uniaxial tensile loading. In order to validate the OSPD-CG model, MD simulations are also performed on the corresponding fully atomistic models. Then the effect of center crack on the fracture of the edge pre-cracked SLGS under uniaxial tensile loading is investigated. Figure 6 presents the OSPD-CG and fully atomistic models of edge pre-cracked SLGS with thickness of 0.34nm. The size of the SLGS is 75nm×100nm and the edge crack size is about 4nm×3.5nm.

(b) Numerical simulation details

In the OSPD-CG model in figure 6a, the SLGS is discretized into uniformly distributed material points with spacing of 0.5nm and contains 30176 material points in total, which is 9.5 times less than the atom number of 285906 in the fully atomistic model in figure 6b. Considering the physical interaction in the fully atomistic system, the radius δ of the horizon in the OSPD-CG model is set as 1 nm. A discussion on the meaning and selection of the PD horizon was made by Bobaru and Hu [53] as well. Based on the stability condition in PD numerical simulation [49] and the consideration of numerical accuracy and computational efficiency, the time step size used in the OSPD-CG method is 5fs which is 5 times larger than the time step of 1fs in MD simulation. In both PD and MD simulations, free boundary conditions are imposed in x and y directions and the pre-cracked SLGS is stretched by moving left and right boundaries with a speed of 3.75m/s along –x and x directions in figure 6, respectively. To avoid abrupt application

of velocity conditions, the initial velocity along x axis in the region between the left and right boundaries is set linearly as -3.75m/s to 3.75m/s from left side to right side in the SLGS. Meanwhile, the left and right boundaries are set as 1nm wide or larger to keep the completeness of the horizon of material points near the left and right boundaries. During the stretch, the temperature of the system is 0K. In addition, the critical energy release rate G_c of the zigzag SLGS is about 9.7 J/m^2 which can be known from MD simulation in which the cutoff is set as 0.185nm [54]. Then according to equation (2.38), the critical stretch in the OSPD-CG model s_c can be obtained as approximately 0.126. In this work, all simulations are performed by using the ThinkStation computer with 8 intel i7 CPUs@3.40GHz and 32GB RAM. It is also observed that the PD simulation of the fracture in edge pre-cracked SLGS needs about 5 hours with only one CPU while the corresponding MD simulation takes almost 22 hours with one CPU. Obviously, larger length scale and time step make PD a more efficient method compared with MD.

(c) Numerical simulation results and discussion

(i) Fracture characteristics of edge pre-cracked SLGS under tensile loading

From PD and fully atomistic MD simulations, the relationships between stress and strain in the fracture process of the edge pre-cracked SLGS under tensile loading are obtained and shown in figure 7. The stress and strain are calculated through $\sigma = F/A$ and $\varepsilon = \Delta L/L_0$, respectively, where F is the force on the right or left boundary along tensile direction, A is the cross sectional area along the right or left boundary, ΔL is the extension of the system along tensile direction and L_0 is the original length of the system along tensile direction.

It can be seen from the figure that the Young's modulus of the edge pre-cracked SLGS in MD and PD simulations are 0.90TPa and 0.86TPa, respectively. The results are in agreement with Hao et al.'s [55] in which the elastic modulus changes between 0.86TPa and 1TPa due to the influence of defects. According to Ref. [56], the fracture strength of the defective graphene varies from 30GPa to 120GPa depending on the defect size, and it drops sharply from 120GPa at very small initial defect size and converges between 30GPa and 60GPa after a certain defect size. In this work it can be observed that the fracture strength and strain of the SLGS in MD and PD simulations are 33GPa and 4.1% and 35GPa and 4.4%, respectively, which are consistent with those in Ref. [56]. The small differences between the current results and those in the mentioned references may be due to the different geometrical size and interatomic potential. Despite the subtle discrepancy in fracture strength and strain in figure 7, the PD simulation results agree very well with the MD simulation results. Therefore, the MD simulation validates the current OSPD-CG model for the edge pre-cracked zigzag SLGS considered in this study.

In figure 8, the final crack propagation patterns in the SLGS obtained from the PD and MD simulations are presented and very similar fracture patterns have been observed by Omeltchenko et al. [52]. Due to high frequency vibration of atoms in the fully atomistic system, especially in the propagation process of cracks, the crack branches are slightly asymmetric about the initial straight crack line in MD simulation results (Figure 8b) compared with the PD simulation results. In order to keep the consistency between the PD and MD simulation results, the crack propagation paths on the left side are

considered.

In figures. 8a and 8b, the initial edge pre-crack propagates for a short distance straightly at first, then the primary crack tip becomes unstable and tends to branch. After the primary crack branching, two secondary cracks form and continue propagating along their own separate directions. When they propagate near the boundaries, the two secondary cracks are reflected by the boundaries and crack turning occurs. Whereafter, the two secondary cracks propagate to the bottom edge of the SLGS. Besides, some obvious and unobvious microcracks are induced as well in the propagation process of the two secondary cracks. In addition, the branching point of the primary crack around which the primary crack tip is unstable and apt to branch is about 7.5nm in front of the pre-crack tip in PD simulation results (Figure 8a) while the corresponding distance is about 7.8nm in MD results (Figure 8b). The position of crack turning point is 11nm from the left edge and 32.5nm from the bottom edge in PD simulation (Figure 8a) while the corresponding distances are 7nm and 33.5nm in MD simulation (Figure 8b). Before and after the crack turning, the angles between the secondary crack paths and horizontal direction are about 62.5 ° and 62 °, respectively, in figure 8a, whereas both of the angles are about 60 ° in figure 8b. Such minor differences can be ascribed to two aspects. On one hand, the hexagonal lattice cell exists in fully atomistic graphene sheets while the fully atomistic system is coarse-grained and discretized into uniform square grids in OSPD-CG model. On the other hand, with coarse-graining techniques a cluster with n atoms is coarse-grained as a material point, thus resulting in $2n$ translational degree of freedoms (DOFs) reduced to 2 in the two dimensional case. As a result, it becomes

stiffer locally at each material point in the OSPD-CG model. Therefore, the fracture patterns such as crack branching point, crack turning point, crack propagation direction and generation of microcracks are slightly different between the PD and MD simulation results as well. Nevertheless, despite such small differences, the fracture characteristics in PD simulation are in good agreement with MD simulation results. In addition, compared with the results based on the quadratic and third-order strain energy density expressions, the fracture characters obtained from the current model can match better with the MD simulation results. Again, the MD simulation gives further confidence to the OSPD-CG model in this study. And the PD results provide a significant insight on multiscale modeling for large nanoscale systems.

(ii) Dynamic fracture process of edge pre-cracked SLGS under tensile loading

Figures. 9 and 10 present the dynamic process of crack propagation and the propagation speed of crack in the edge pre-cracked SLGS under tensile loading, respectively. Here, Δt stands for the time period after the initial pre-crack begins to propagate.

When $\Delta t = 0\text{ps}$ in figure 9, the initial pre-crack begins to propagate. Before this moment, the SLGS is stretched continuously, which results in accumulation of more and more strain energy around the edge pre-crack tip. Propagation of the initial pre-crack initiates as soon as the strain energy accumulates to a certain degree and the propagation speed quickly reaches an average value of 5Km/s, which can be seen from the PD results in figure 10. With this speed, the primary crack continues propagating until $\Delta t = 1.75\text{ps}$ at which it tends to branch into two secondary cracks (Figure 9). Besides, it can be seen that the propagation speed of the primary crack becomes higher and the

average value is close to 8Km/s (Figure 10), that the damage zone near the branching point becomes a little thicker ($\Delta t = 1.75\text{ps}$ in figure 9) due to generation of some unobvious microcracks in the crack propagation process when the crack velocity is higher than 8Km/s and that the strain energy around the primary crack tip also reaches another level. These may be the reasons why the primary crack tends to branch at this moment. After the primary crack branching, the two secondary cracks keep moving along their own directions with an average speed of about 8Km/s (Figure 10). In this process, many unobvious microcracks form as well ($\Delta t = 6.75\text{ps}$ in figure 9). Meanwhile, it can also be observed from the strain energy distribution that there are waves continuously emitting from the moving crack tips. From $\Delta t = 6.75\text{ps}$ to $\Delta t = 10.25\text{ps}$ (Figure 9), some obvious microcracks sprout from the moving tips of the two secondary cracks due to the interaction between the waves reflected by the boundaries and the moving crack tips. The interaction becomes more and more intensified with the crack tips moving more and more close to the boundaries. Consequently, such kind of microcracks become more and more obvious during this period and can be seen as tertiary cracks due to branching of the secondary cracks. However, they only grow for a very short distance because their growth becomes not energetically favorable for the reason that the growth of the secondary cracks dissipates more energy and there's not enough energy for those microcracks to propagate any more. At $\Delta t = 10.25\text{ps}$ (Figure 9), the two secondary cracks propagate near the boundaries and begin to branch. However, the branches closer to the boundaries are blocked by the boundaries and do not continue propagating. Therefore, it seems that the secondary

cracks are reflected by the boundaries and crack turnings happen ($\Delta t = 13.5\text{ps}$ in figure 9). From figure 10, it can be seen that the crack tip velocity is reduced to about 6.3Km/s before crack turning because of the influence of the boundaries. Also, the stress increases during this crack turning stage in figure 7, which means crack turning needs extra energy flowing into the system in the propagation process of cracks. After turning of the secondary cracks, they keep propagating at average speed of 7.2Km/s (Figure 10) and branch at $\Delta t = 13.5\text{ps}$ (Figure 9). Then the two branches propagate to the bottom edge at $\Delta t = 14.75\text{ps}$ and the strain energy is also released (Figure 9). In addition, similar phenomena, especially the interaction between the reflected waves and the moving crack tips, can be observed in fully atomistic MD simulations.

As shown in figure 10, the crack velocities in both MD and PD simulations are very close to each other. Moreover, the crack velocity in PD simulation agrees well with that in Ref. [52], in which the average crack propagation speed is between 6Km/s and 8Km/s. The crack velocity in MD simulation in this work is slightly higher and the maximum value is close to 10Km/s, which can be attributed to the effect of interatomic potential functions.

(iii) Fracture of center pre-cracked SLGS under tensile loading

Beside the fracture of the edge pre-cracked SLGS, the fracture of SLGS with vertically center crack of different lengths under uniaxial tensile loading is studied. Figure 11 shows the effect of center crack length on the fracture strength and the crack propagation patterns.

In figure 11, it can be seen that the vertically center crack of different lengths has

big influence on the fracture strength of SLGS. With the length of the center crack increasing from 1nm to 15nm, the fracture strength of SLGS decreases from about 55GPa to 22GPa. Especially, the fracture strength of SLGS is around 40GPa when the length of center crack is about 3.5nm. Compared with the edge pre-cracked SLGS case in which the fracture strength is about 35GPa and the edge crack length is 3.5nm, it is shown that the edge crack has more significant effect on the fracture of SLGS. In addition, it is observed that the fracture of the center pre-cracked SLGS initiates from both the left and right fixed boundaries at the upper and lower edges when the center crack length is 1nm or smaller and such form is also consistent with MD simulation result. The propagation forms in SLGS are similar with each other when the center crack length is longer than 2nm. In the first stage, the center crack begins to propagate straightly from its two ends for a small distance. The two primary cracks branch into two secondary cracks with an angle of almost 60° which next extend to the upper and lower edges, respectively, in the second stage. Microcracks generate more or less in this stage. However, different from the propagation of edge crack, the crack turning stage does not occur in all center pre-cracked SLGS for the reason that the center crack may not have enough long path to go before it propagates near the left and right boundaries compared with the edge crack or the secondary cracks have spread out from the upper and lower edges before they are blocked and reflected by the right and left boundaries. It is also found that the branching point of the primary crack is more and more far away from the initial center crack ends with the length of center crack increasing. This is for the reason that more energy can be released out from the crack surface of the longer

crack during the initial crack propagation process in the first stage of crack propagation and it may lead to the primary crack propagating for longer distance to reach the critical crack tip velocity and strain energy around the moving crack tip which are necessary for the branching of the primary crack as mentioned above.

In order to show the consistency of the established OSPD-CG model and the known MD method in the fracture simulation of center pre-cracked SLGS, the SLGS with a 5nm long center crack is chosen to perform another atomistic MD simulation. Figure 12 presents the corresponding fracture forms of SLGS obtained from OSPD-CG and MD simulations. It is shown that the main crack propagation characteristics in both the simulation results such as the branching of primary crack with an angle of about 60°, the positions of branching points of the primary cracks initiating from the center crack (about 6.5nm away from each end of the center crack) and the generation of microcracks in the propagation process of the secondary cracks are significantly consistent with each other. Moreover, the fracture strength and strain are also very close in both simulations, which are about 35 GPa and 4.5%.

(iv) Effect of center crack on the fracture of edge pre-cracked SLGS under tensile loading

In this section, the effect of vertically center crack of different lengths on the fracture of the edge pre-cracked SLGS in section 4.3.1 is investigated and the results such as the fracture strength and fracture forms are shown in figure 13.

It shows that the center crack has little effect on the fracture strength of the edge pre-cracked SLGS when the length of center crack is less than 5nm and the fracture

strength is close to 35GPa. Besides, the fracture initiates from the edge crack tip. When the length of center crack is larger than 5nm, the fracture strength of edge pre-cracked SLGS decreases largely with the length of center crack increasing and the fracture initiates from the center crack ends. Moreover, the fracture form is obviously affected by the vertically center crack. When the center crack is 1nm long, as shown in figure 13, the fracture form is almost the same as that of the edge pre-cracked SLGS without center crack presented in figure 8. For the edge pre-cracked SLGS with a 2nm long center crack, the fracture pattern is a little different from the one with 1nm long center crack. After the primary crack from the initial edge crack branching, the two secondary cracks again branches into two tertiary cracks at the level of the center crack, respectively. Then the four tertiary cracks propagate to the lower edge. In this process, the two tertiary cracks along the paths of the two secondary cracks are blocked but not reflected by the left and right boundaries and then propagate vertically due to the continuous propagation of the other two tertiary cracks. When the length of center crack is between 3nm to 5nm, the two secondary cracks propagate to the range which is near the lower end of center crack vertically and then stop propagating any more. Then the fracture initiates from the center crack and the crack begins to propagate from the lower end of the center crack (See the crack propagation paths when the center crack is 5nm long in figure 13). When the center crack is longer than 5nm, the fracture form is like the one in which the center crack is 8nm long in figure 13. It is also very similar with the fracture form of the center pre-cracked SLGS (Figure 12) in the previous section.

Therefore, the fracture of the edge pre-cracked SLGS with center crack is mainly

dominated by the edge crack rather than by the center crack with length less than 5nm. On the other hand, the fracture is dominated by the center crack with length larger than 5nm.

4. Conclusion

An OSPD-CG model is developed by generalizing the linear elastic PD model to a nonlinear one through extending the original invariable PD parameters to quadratic expressions which depend on the dilatation and bond stretch terms. The PD parameters in the OSPD-CG model are derived completely from the fully atomic scale system by using the energy conservation approach, which is different from the original method in which the PD parameters are obtained based on CCM theory. Then, the newly developed OSPD-CG model is employed for simulation of crack propagation in zigzag SLGS which is a physical nonlinear material. Based on the developed OSPD-CG model, the fracture mechanisms in pre-cracked SLGS under uniaxial tensile loading are revealed qualitatively through analysis of the crack tip velocity and strain energy around moving crack tip. In contrast to MD method, the current OSPD-CG model can be used for investigating larger scale systems.

Ethics statement

Not applicable.

Data accessibility statement

Some videos supporting this paper have been uploaded as part of the supplementary material.

Competing interests statement

We have no competing interests.

Authors' contributions

Liu, Wang and He conceived the model and finished the manuscript. Liu implemented the calculations and numerical simulations. Sun and Oterkus provided suggestions for the improvement of this work. All authors gave final approval for publication.

Acknowledgements

Not applicable.

Funding statement

This research work was fully supported by the City University of Hong Kong (Grant No. 7004368 and 7004878) and the National Nature Science Foundation of China (11372281).

References

[1] Matyba, P., et al., Graphene and mobile ions: the key to all-plastic, solution-processed light-emitting devices. ACS NANO, 2010, 4(2): 637-42. (doi: 10.1021/nn9018569)

[2] Stoller, M.D., et al., Graphene-based ultracapacitors. NANO LETT, 2008, 8(10): 3498-502. (doi: 10.1021/nl802558y)

[3] Surwade, S.P., et al., Water desalination using nanoporous single-layer graphene. NAT NANOTECHNOL, 2015, 10(5): 459-64. (doi:10.1038/nnano.2015.37)

[4] Rafiee, M.A., Graphene-based composite materials. 2011, Rensselaer Polytechnic Institute.

[5] Borodich, F.M. and B.A. Galanov, Contact probing of stretched membranes and adhesive interactions: graphene and other two-dimensional materials. P ROY SOC A-MATH PHY, 2016, 472: 20160550. (doi: 10.1098/rspa.2016.0550)

[6] Kitipornchai, S., X.Q. He and K.M. Liew, Continuum model for the vibration of

multilayered graphene sheets. PHYS REV B, 2005, 72(7): 75443. (doi: 10.1103/PhysRevB.72.075443)

[7] He, X.Q., S. Kitipornchai and K.M. Liew, Resonance analysis of multi-layered graphene sheets used as nanoscale resonators. NANOTECHNOLOGY, 2005, 16(10): 2086-2091. (doi: stacks.iop.org/Nano/16/2086)

[8] Reddy, C.D., S. Rajendran and K.M. Liew, Equilibrium configuration and continuum elastic properties of finite sized graphene. NANOTECHNOLOGY, 2006, 17(3): 864-870. (doi: stacks.iop.org/Nano/17/864)

[9] Zou, B., et al., The Young's moduli of three types of carbon allotropes: a molecular mechanics model and a finite-element method. P ROY SOC A-MATH PHY, 2016, 472: 20150628. (doi: 10.1098/rspa.2015.0628)

[10] Zhang, T., X. Li and H. Gao, Defects controlled wrinkling and topological design in graphene. J MECH PHYS SOLIDS, 2014, 67: 2-13. (https://doi.org/10.1016/j.jmps.2014.02.005)

[11] Zhao, H. and N.R. Alurua, Temperature and strain-rate dependent fracture strength of graphene. J APPL PHYS, 2010, 108(6): 64321. (doi: 10.1063/1.3488620)

[12] Ansari, R., et al., Fracture analysis of monolayer graphene sheets with double vacancy defects via MD simulation. SOLID STATE COMMUN, 2011, 151(17): 1141-1146. (doi: 10.1016/j.ssc.2011.05.021)

[13] Wang, M.C., et al., Effect of defects on fracture strength of graphene sheets. COMP MATER SCI, 2012, 54: 236-239. (doi: 10.1016/j.commatsci.2011.10.032)

[14] Dewapriya, M. and S.A. Meguid, Atomistic simulations of nanoscale crack-vacancy interaction in graphene. CARBON, 2017, 125: 113-131. (doi: 10.1016/j.carbon.2017.09.015)

[15] Zhang, T., et al., Flaw Insensitive Fracture in Nanocrystalline Graphene. NANO LETT, 2012, 12(9): 4605-4610. (DOI: 10.1021/nl301908b)

[16] Zhang, T., X. Li and H. Gao, Fracture of graphene: a review. INT J FRACTURE, 2015, 196(1-2): 1-31. (doi: 10.1007/s10704-015-0039-9)

[17] Rajasekaran, G., P. Narayanan and A. Parashar, Effect of Point and Line Defects on Mechanical and Thermal Properties of Graphene: A Review. CRIT REV SOLID STATE, 2016, 41(1): 47-71. (doi: 10.1080/10408436.2015.1068160)

[18] Tsai, J., S. Tzeng and Y. Tzou, Characterizing the fracture parameters of a graphene sheet using atomistic simulation and continuum mechanics. INT J SOLIDS STRUCT, 2010, 47(3): 503-509. (doi: 10.1016/j.ijsolstr.2009.10.017)

[19] Xu, M., et al., A coupled quantum/continuum mechanics study of graphene fracture. INT J FRACTURE, 2012, 173(2): 163-173. (doi: 10.1007/s10704-011-9675-x)

[20] Gracie, R. and T. Belytschko, Concurrently coupled atomistic and XFEM models

for dislocations and cracks. INT J NUMER METH ENG, 2009, 78(3): 354-378. (doi: 10.1002/nme.2488)
[21] Cranford, S., D. Sen and M.J. Buehler, Meso-origami: folding multilayer graphene sheets. APPL PHYS LETT, 2009, 95(12): 123121. (doi: 10.1063/1.3223783)
[22] Ruiz, L., et al., A coarse-grained model for the mechanical behavior of multi-layer graphene. CARBON, 2015, 82: 103-115. (doi: 10.1016/j.carbon.2014.10.040)
[23] Shang, J., Q. Yang and X. Liu, A New Coarse-Grained Model and Its Implementation in Simulations of Graphene Assemblies. J CHEM THEORY COMPUT, 2017, 13(8): 3706-3714. (doi: 10.1021/acs.jctc.7b00051)
[24] Silling, S.A., Reformulation of elasticity theory for discontinuities and long-range forces. J MECH PHYS SOLIDS, 2000, 48(1): 175-209. (doi: 10.1016/S0022-5096(99)00029-0)
[25] Silling, S.A., et al., Peridynamic States and Constitutive Modeling. J ELASTICITY, 2007, 88(2): 151-184. (doi: 10.1007/s10659-007-9125-1)
[26] Silling, S.A., Dynamic fracture modeling with a meshfree peridynamic code, in Proceedings Second MIT Conference on Compurational Fluid and Solid Mechanics. 2003, 641-644. (doi: 10.1016/B978-008044046-0.50157-3)
[27] Ha, Y.D. and F. Bobaru, Characteristics of dynamic brittle fracture captured with peridynamics. ENG FRACT MECH, 2011, 78(6): 1156-1168. (doi: /10.1016/j.engfracmech.2010.11.020)
[28] Vazic, B., et al., Dynamic propagation of a macrocrack interacting with parallel small cracks. AIMS Materials Science, 2017, 4(1): 118-136. (doi: 10.3934/matersci.2017.1.118)
[29] Liu, M., Q. Wang and W. Lu, Peridynamic simulation of brittle-ice crushed by a vertical structure. INT J NAV ARCH OCEAN, 2016, 9(2): 209-218. (doi: 10.1016/j.ijnaoe.2016.10.003)
[30] Lai, X., et al., Peridynamics simulations of geomaterial fragmentation by impulse loads. INT J NUMER ANAL MET, 2015, 39(12): 1304-1330. (doi: 10.1002/nag.2356)
[31] Agwai, A., I. Guven and E. Madenci, Crack propagation in multilayer thin-film structures of electronic packages using the peridynamic theory. MICROELECTRON RELIAB, 2011, 51(12): 2298-2305. (doi; 10.1016/j.microrel.2011.05.011)
[32] Taylor, M., et al., Peridynamic Modeling of Ruptures in Biomembranes. PLOS ONE, 2016, 11(11): e165947. (doi: 10.1371/journal.pone.0165947)
[33] Zhu, N., D. De Meo and E. Oterkus, Modelling of granular fracture in polycrystalline materials using ordinary state-based peridynamics. MATERIALS, 2016, 9(12): 977. (doi: 10.3390/ma9120977)
[34] De Meo, D., N. Zhu and E. Oterkus, Peridynamic modeling of granular fracture in

polycrystalline materials. Journal of Engineering Materials and Technology, 2016, 138(4): 41008. (doi: 10.1115/1.4033634)

[35] Oterkus, E., et al., Utilization of Peridynamic Theory for Modeling at the Nano-Scale. Nanopackaging: From Nanomaterials to the Atomic Scale, 2015: 1-16. (doi: 10.1007/978-3-319-21194-7_1)

[36] Bobaru, F., et al., Peridynamic 3D models of nanofiber networks and carbon nanotube-reinforced composites. AIP, 2004, 712(1): 1565-1570. (doi: 10.1063/1.1766752)

[37] Bobaru, F., S.A. Silling and H. Jiang, Peridynamic fracture and damage modeling of membranes and nanofiber networks, XI Int. Conf. Fract. 2005.

[38] Bobaru, F., Influence of van der Waals forces on increasing the strength and toughness in dynamic fracture of nanofibre networks: a peridynamic approach. MODEL SIMUL MATER SC, 2007, 15(5): 397-417. (doi: 10.1088/0965-0393/15/5/002)

[39] Celik, E., et al., Mechanical characterization of ultra-thin films by combining AFM nanoindentation tests and peridynamic simulations, in IEEE Electronic Components and Technology Conference. 2009, IEEE, 262-268. (doi: 10.1109/ECTC.2009.5074026)

[40] Ebrahimi, S., D. Steigmann and K. Komvopoulos, Peridynamics analysis of the nanoscale friction and wear properties of amorphous carbon thin films. J MECH MATER STRUCT, 2015, 10(5): 559-572. (doi: 10.2140/jomms.2015.10.559)

[41] Gerstle, W.H., INTRODUCTION TO PRACTICAL PERIDYNAMICS: Computational Solid Mechanics Without Stress and Strain. 2015: World Scientific Publishing Co Inc.

[42] Bobaru, F., et al., Handbook of Peridynamic Modeling. 2016: CRC Press.

[43] Madenci, E. and E. Oterkus, Peridynamic Theory and Its Applications. 2014: Springer.

[44] Martowicz, A., et al., Peridynamics as an analysis tool for wave propagation in graphene nanoribbons. SPIE Smart Structures and Materials+Nondestructive Evaluation and Health Monitoring. International Society for Optics and Photonics. 2015, (doi: 10.1117/12.2084312)

[45] Madenci, E., Peridynamic integrals for strain invariants of homogeneous deformation. ZAMM - Journal of Applied Mathematics and Mechanics / Zeitschrift für Angewandte Mathematik und Mechanik, 2017, 97(10): 1236-1251. (https://doi.org/10.1002/zamm.201600242)

[46] Silling, S.A., A coarsening method for linear peridynamics. INT J MULTISCALE COM, 2011. 9(6): 609-622. (doi: 10.1615/IntJMultCompEng.2011002674)

[47] Liu, W. and J.W. Hong, Discretized peridynamics for linear elastic solids. COMPUT MECH, 2012, 50(5): 579-590. (doi: 10.1007/s00466-012-0690-1)

[48] Kalosakas, G., et al., In-plane force fields and elastic properties of graphene. J APPL PHYS, 2013, 113(13): 134307. (do: 10.1063/1.4798384)
[49] Silling, S.A. and E. Askari, A meshfree method based on the peridynamic model of solid mechanics. COMPUT STRUCT, 2005, 83(17): 1526-1535. (doi: 10.1016/j.compstruc.2004.11.026)
[50] Foster, J.T., S.A. Silling and W. Chen, An energy based failure criterion for use with peridynamic states. INT J MULTISCALE COM, 2011, 9(6): 675-688. (doi: 10.1615/IntJMultCompEng.2011002407)
[51] Hwangbo, Y., et al., Fracture Characteristics of Monolayer CVD-Graphene. 2014, 4: 4439. (doi: 10.1038/srep04439)
[52] Omeltchenko, A., et al., Crack front propagation and fracture in a graphite sheet: a molecular-dynamics study on parallel computers. PHYS REV LETT, 1997, 78(11): 2148. (doi: 10.1103/PhysRevLett.78.2148)
[53] Bobaru, F. and W. Hu, The meaning, selection, and use of the peridynamic horizon and its relation to crack branching in brittle materials. INT J FRACTURE, 2012, 176(2): 215-222. (doi: 10.1007/s10704-012-9725-z)
[54] Xiao, J.R., J. Staniszewski and J.W. Gillespie, Fracture and progressive failure of defective graphene sheets and carbon nanotubes. COMPOS STRUCT, 2009, 88(4): 602-609. (doi: 10.1016/j.compstruct.2008.06.008)
[55] Hao, F., D. Fang and Z. Xu, Mechanical and thermal transport properties of graphene with defects. APPL PHYS LETT, 2011, 99(4): 41901. (doi: 10.1063/1.3615290)
[56] Budarapu, P.R., et al., Crack propagation in graphene. J APPL PHYS, 2015, 118(6): 64307. (doi: 10.1063/1.4928316)
[57] Colombo L, Giordano S. Nonlinear elasticity in nanostructured materials. REP PROG PHYS, 2011, 74(11): 116501.

List of figure captions

Figure 1 Horizon of material points *k* and *j* in undeformed (reference) and deformed configurations and force density vectors between material points in the horizon, *H*.

Figure 2 Schematic of the OSPD-CG model for the fully atomistic graphene model and the states after deformation under various loading conditions. The colored circle stands for the horizon of the corresponding material point. The magnified inset shows a

cluster atoms coarse-grained as a material point in PD.

Figure 3 Schematics of different loading conditions applied on the fully atomistic SLGS cell. (a) Expansion, (b) Uniaxial extension, (c) Shear.

Figure 4 The relationships between the strain energy density and strain of the fully atomistic SLGS cell under different loading conditions.

Figure 5 Evaluation of the energy release rate in PD model.

Figure 6 The OSPD-CG and fully atomistic graphene models. (a) OSPD-CG, (b) Fully atomistic. The magnified insets show the pre-crack in both models.

Figure 7 Stress-strain relationships in the fracture process. The inset in the magenta colored region shows the variations in the crack turning stage.

Figure 8 Crack propagation patterns characterized by local damage index in PD and MD simulations. (a) OSPD-CG, (b) MD.

Figure 9 Dynamic crack propagation patterns characterized by local damage index (first and third row) and the corresponding distribution of strain energy (second and fourth row) in the pre-cracked SLGS under tensile loading at different time. (Supplementary movie 1 shows the dynamic crack propagation and reveals the interaction between cracks in the propagating process by using the strain energy distribution.)

Figure 10 Crack tip velocities in the edge pre-cracked SLGS under tensile loading.

Figure 11 The fracture strength of SLGS with vertically center crack of different

lengths and the corresponding crack propagation forms.

Figure 12 The crack propagation patterns characterized by local damage index in SLGS when the length of center crack is 5nm. (a) OSPD-CG, (b) MD.

Figure 13 The fracture strength of edge pre-cracked SLGS with vertically center crack of different lengths and the corresponding crack propagation patterns. (Supplementary movies 2~5 show the fracture process of the edge pre-cracked SLGS with centered crack 1nm, 2nm, 5nm and 8nm long and reveal the interaction between cracks by using the strain energy distribution.)

List of table captions

Table I The PD parameters in the OSPD-CG model of SLGS

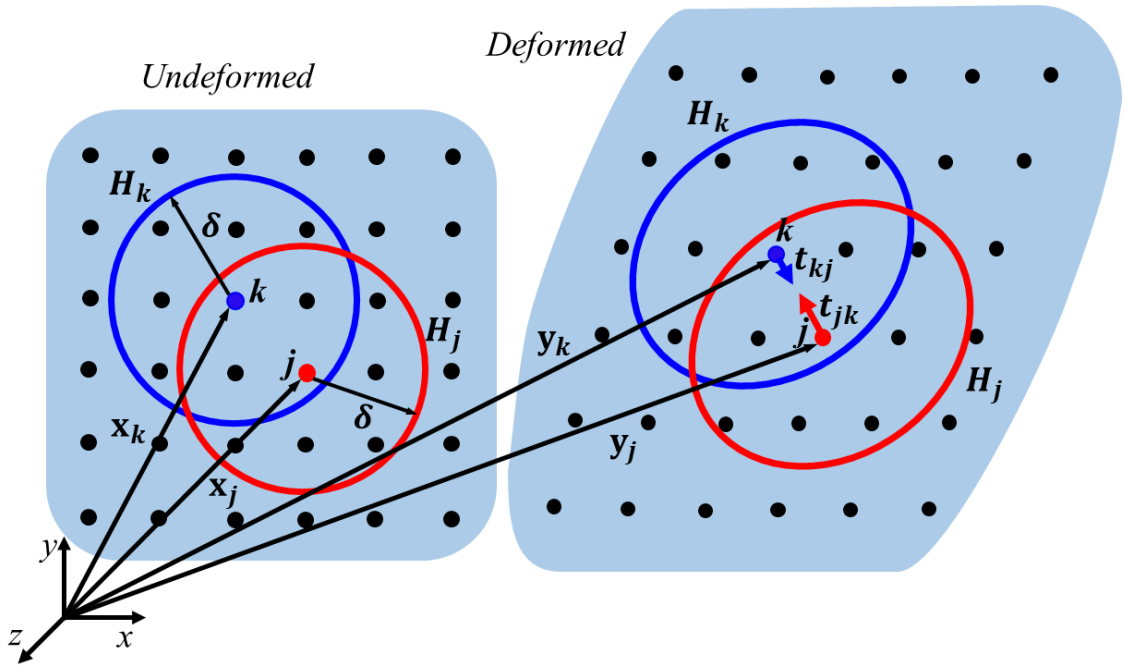

Figure 1

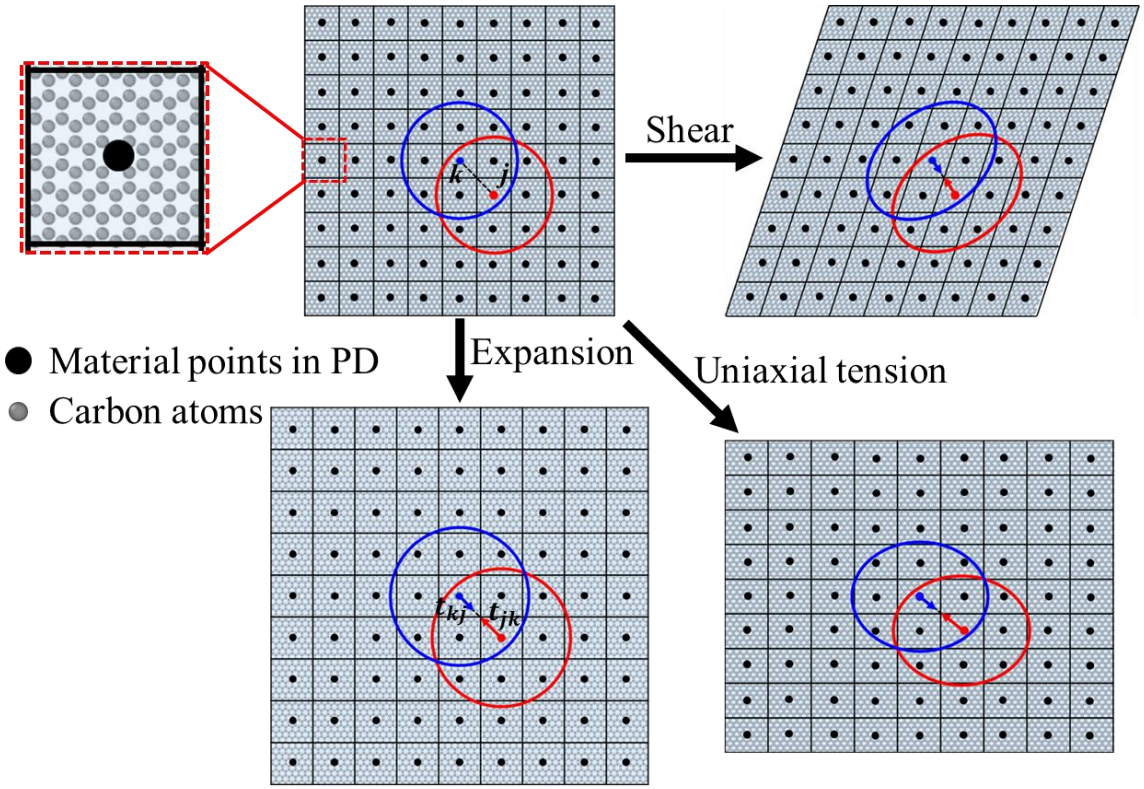

Figure 2

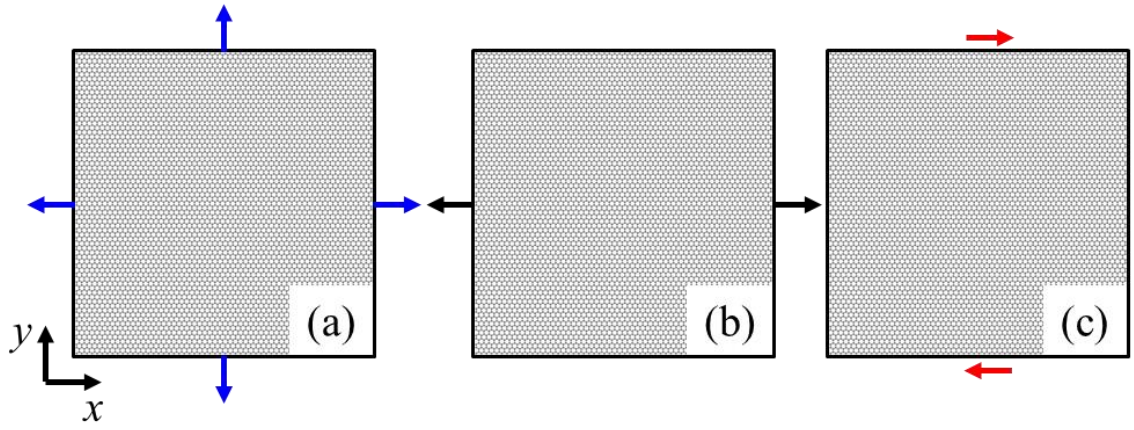

Figure 3

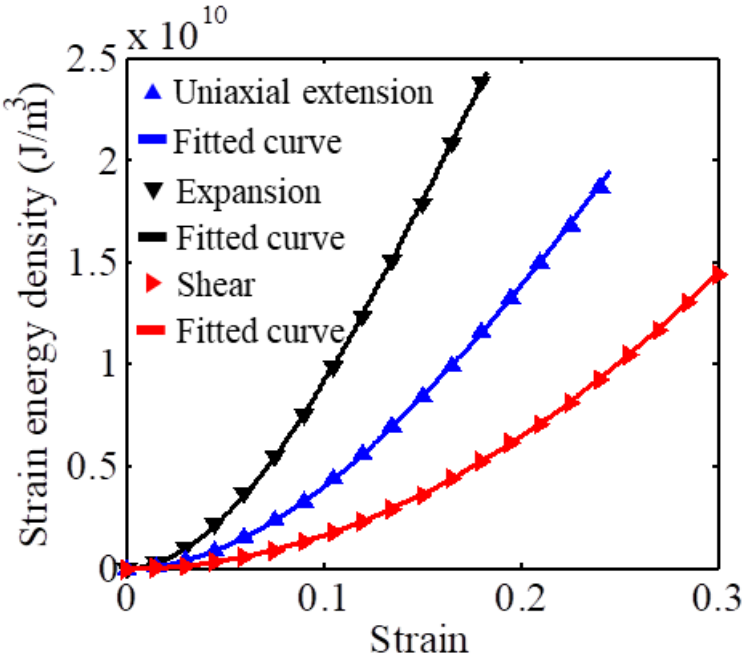

Figure 4

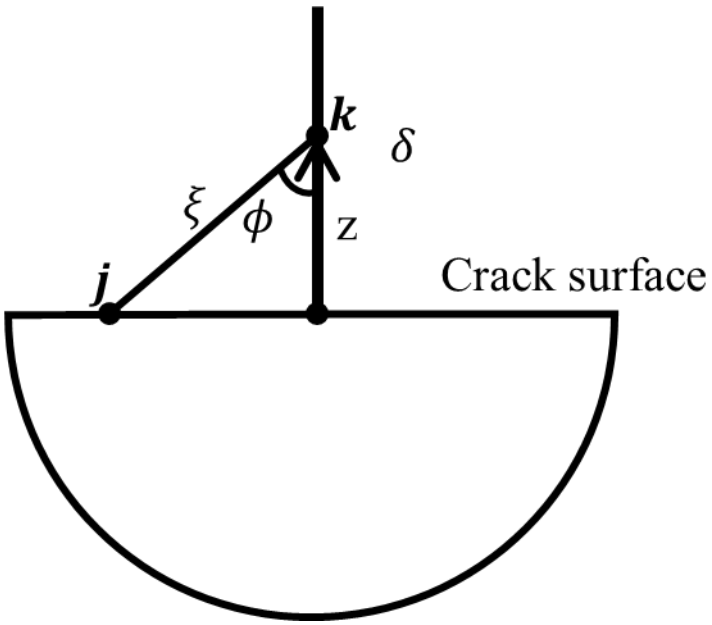

Figure 5

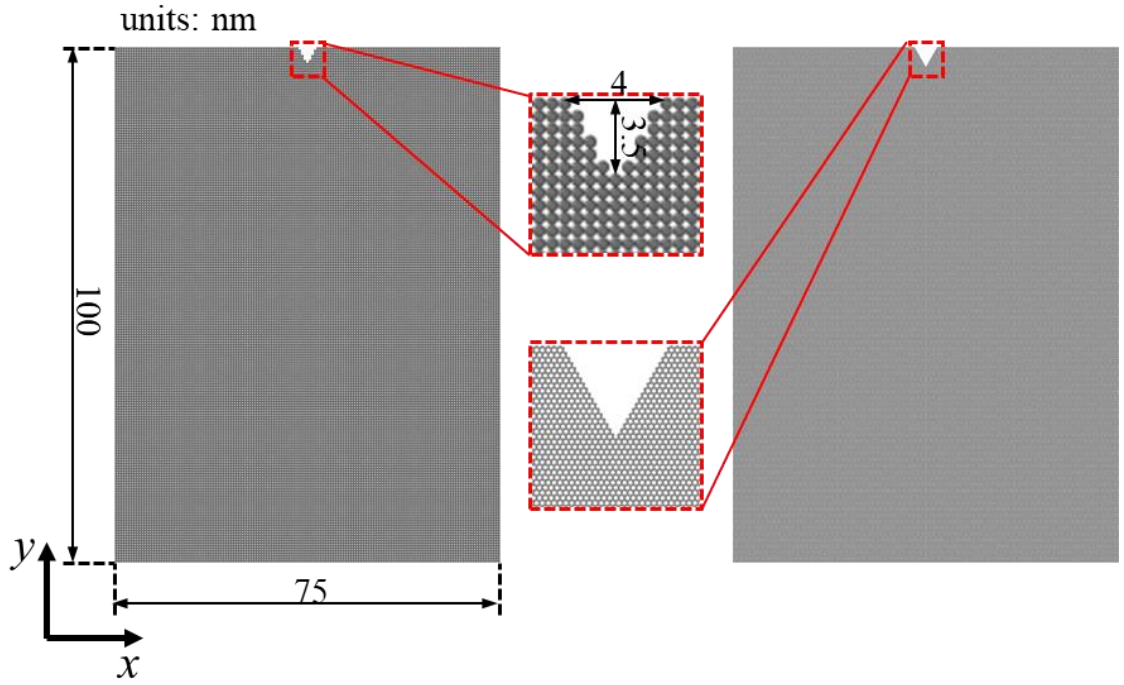

Figure 6

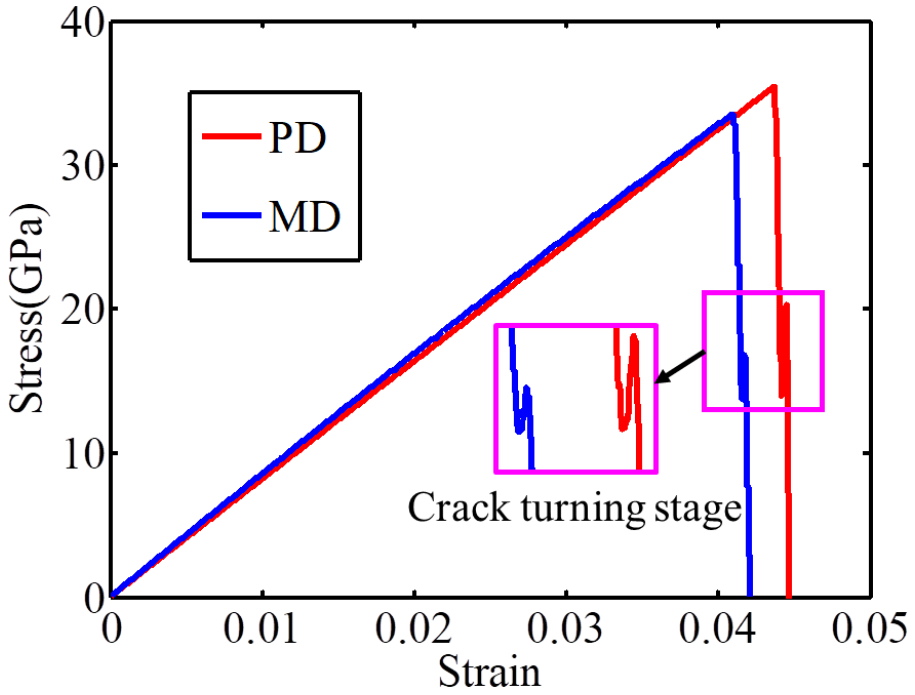

Figure 7

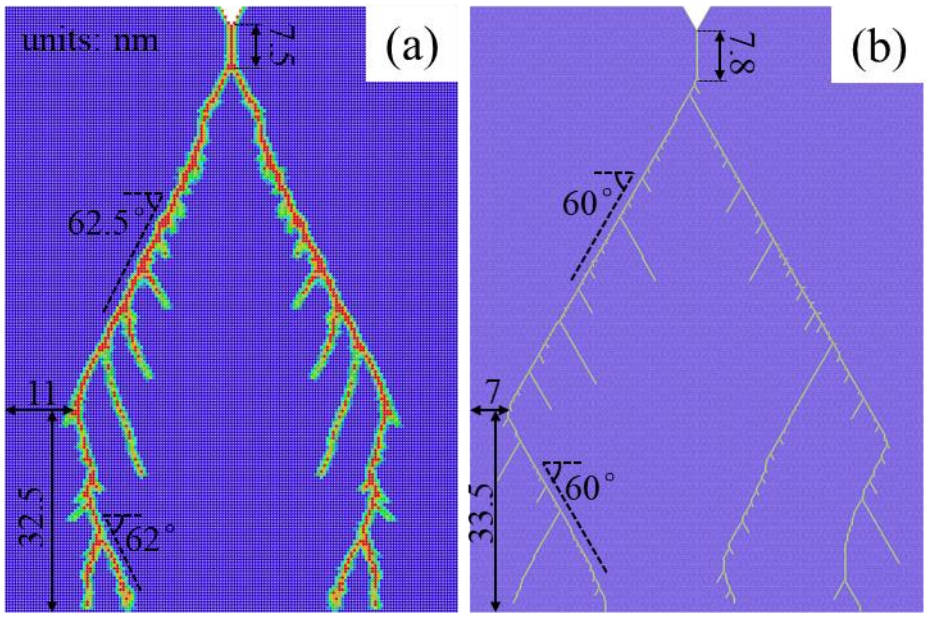

Figure 8

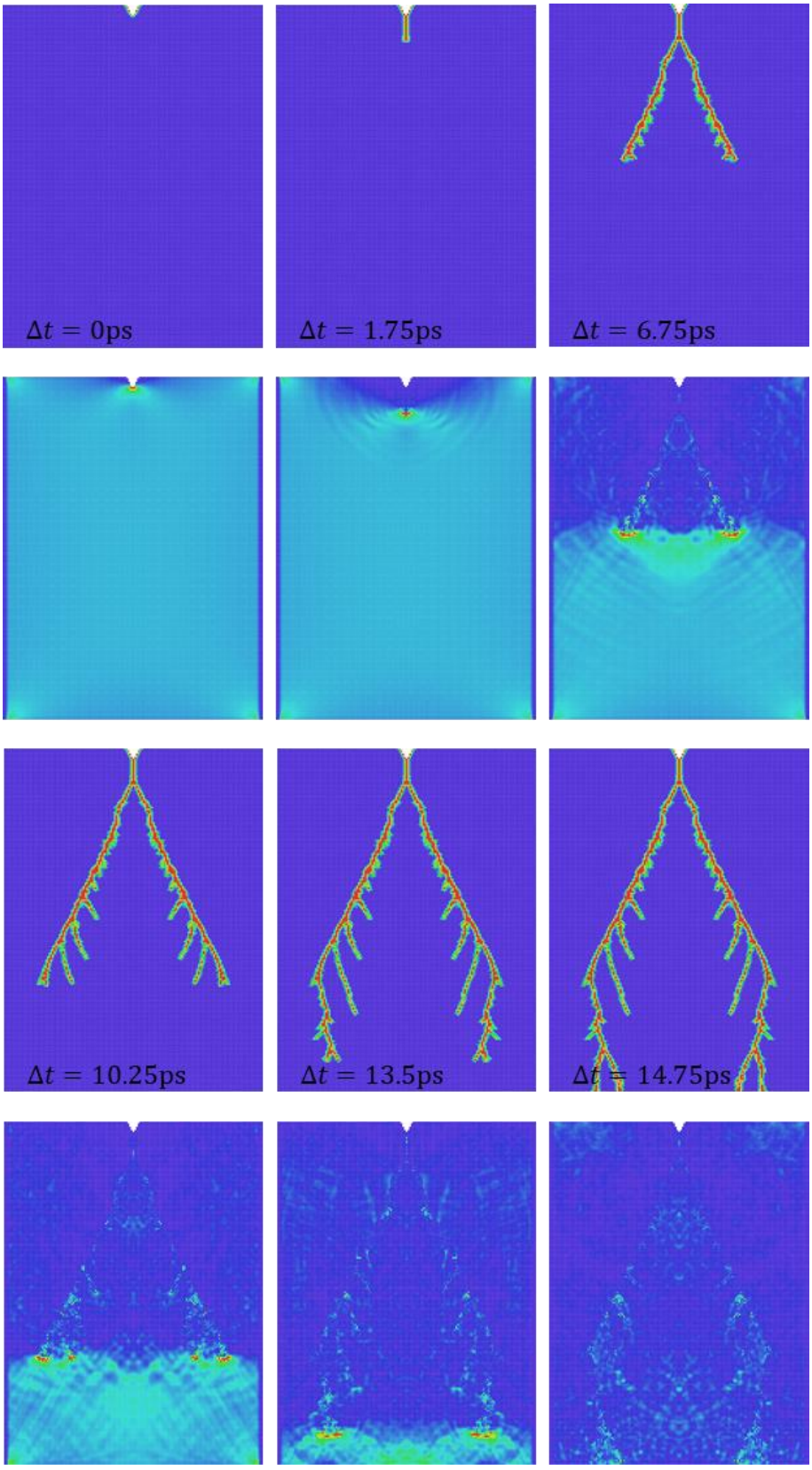
$\Delta t = 0$ps
$\Delta t = 1.75$ps
$\Delta t = 6.75$ps
$\Delta t = 10.25$ps
$\Delta t = 13.5$ps
$\Delta t = 14.75$ps

Figure 9

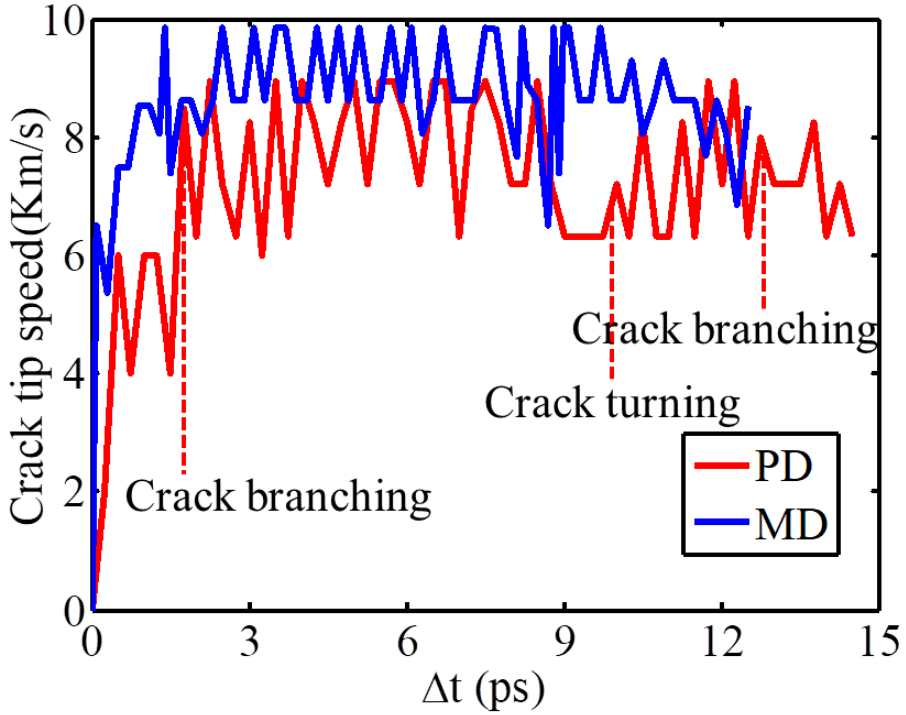

Figure 10

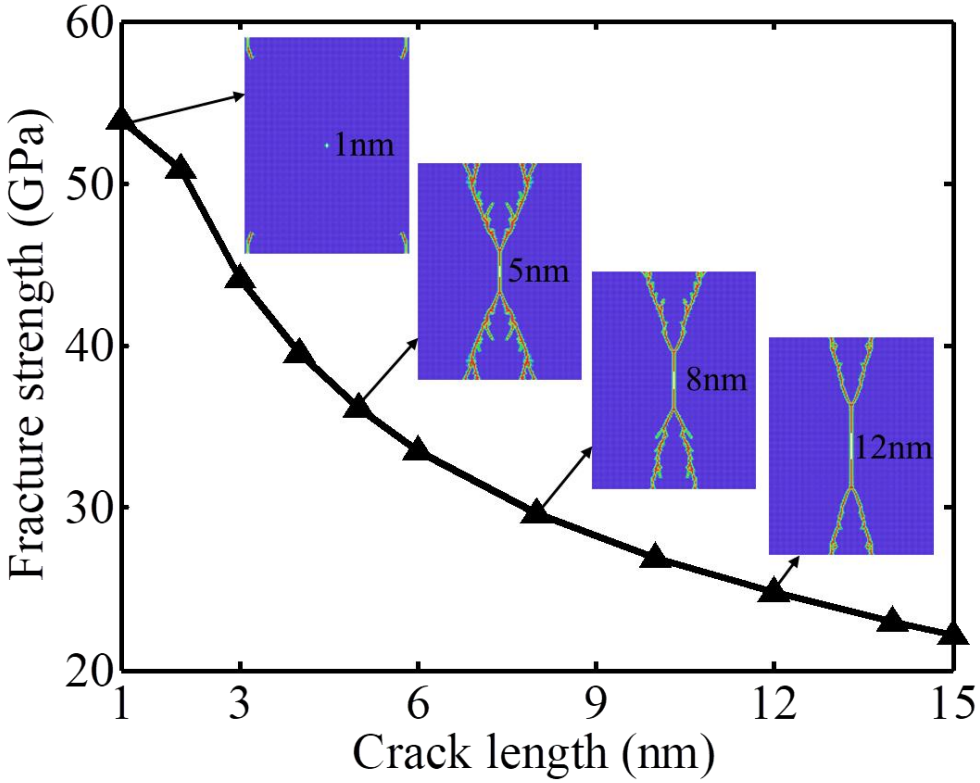

Figure 11

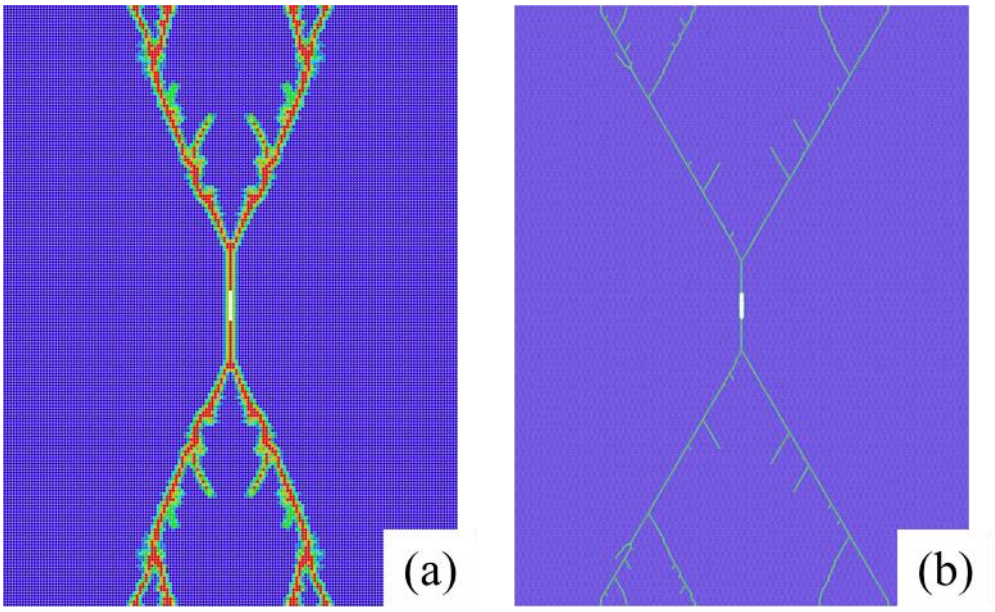

Figure 12

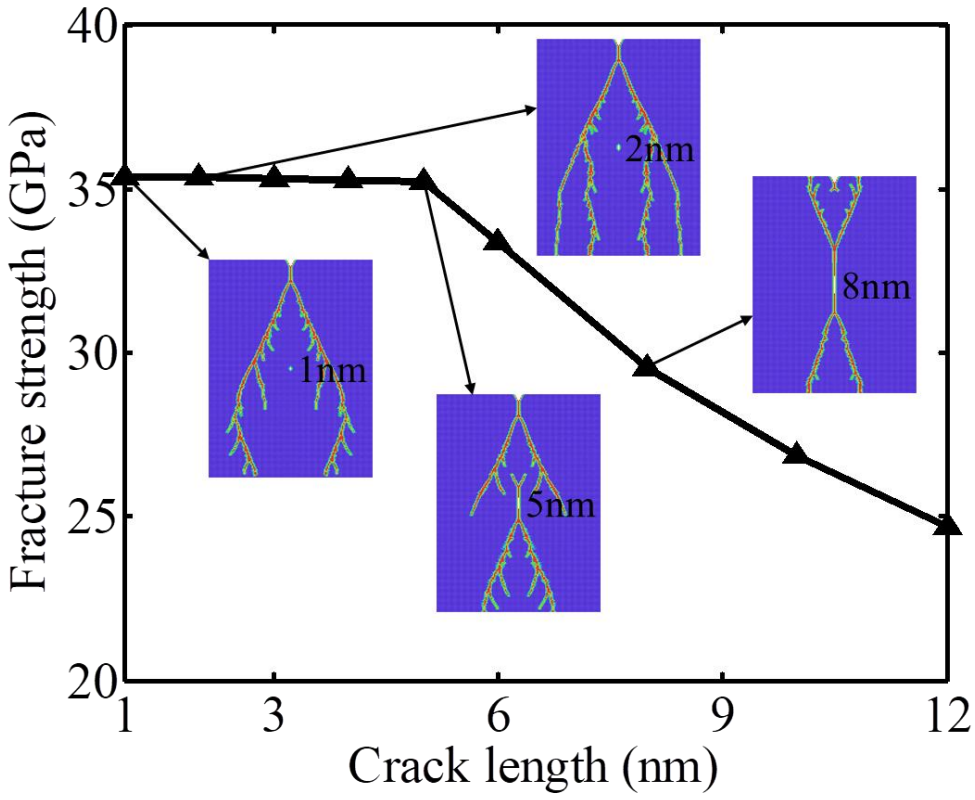

Figure 13

Table I

	Dilatation	Bond stretch
	$a(\theta_k) = a_1\theta_k + a_0$	$b(\theta_k) = b_1\theta_k + b_0$
$\bar{d} = \frac{3}{\pi h \delta^4}$	$a_0 = -3.85 \times 10^{10}$	$b_0 = \frac{1.93 \times 10^{12}}{\pi h \delta^4}$
	$a_1 = 1.89 \times 10^{11}$	$b_1 = \frac{-2.80 \times 10^{12}}{\pi h \delta^4}$